



Kinetic analysis of crystallization process in $[(\text{Fe}_{0.9}\text{Ni}_{0.1})_{77}\text{Mo}_5\text{P}_9\text{C}_{7.5}\text{B}_{1.5}]_{100-x}\text{Cu}_x$ ($x = 0.1$ at.%) BMG

Non-isothermal condition

Z. Jaafari¹ · A. Seifoddini¹ · S. Hasani¹ · P. Rezaei-Shahreza¹

Received: 25 February 2018 / Accepted: 11 May 2018 / Published online: 21 May 2018
© Akadémiai Kiadó, Budapest, Hungary 2018

Abstract

The present work demonstrates the results of crystallization kinetic of $[(\text{Fe}_{0.9}\text{Ni}_{0.1})_{77}\text{Mo}_5\text{P}_9\text{C}_{7.5}\text{B}_{1.5}]_{100-x}\text{Cu}_x$ ($x = 0.1$ at.%) amorphous metallic alloy during non-isothermal annealing done by differential thermal analysis at various heating rates of 10, 20, and 40 K min⁻¹ up to 1473 K. The results showed that by increasing the crystallization temperature, some crystalline phases including α -Fe, γ -Fe, FeNi₂P, and Fe₃C were formed. In addition, the volume fraction of crystalline phases increased from 9.2 to 20.2%, confirming the presence of crystalline phases by FE-SEM results. To calculate the activation energy (E_a), which is approximately independent of “ α ” in a wide range, some isoconversional methods such as Starink and Friedman were used for various crystallization steps. Moreover, the invariant kinetic parameters including IKP method and fitting models were used to calculate the empirical kinetic triplets [E , A , and $g(\alpha)$]. IKP and Fitting methods are in a good agreement with each other to determine the kinetic mechanism at each crystallization stage. Therefore, to ensure the IKP results, the mechanism of four crystallization peaks was determined using a fitting method. Finally, it was found that the first, second, third, and fourth crystallization stages were controlled by A_4 , A_4 , A_4 , and P_4 models, respectively.

Keywords Amorphous alloys · Crystallization · Non-isothermal kinetics · Nanocomposite · Nanocrystals

Introduction

The Fe-based bulk metallic glasses (BMGs) have attracted too much attention by exhibiting impressive mechanical properties [1], excellent corrosion resistance [2–6], and good magnetic properties [7–10] to use in widespread applications such as sensors [11], transformers [12, 13], and magnetic tapes [14]. However, these BMGs exhibit a limited plasticity at room temperature and are a common example of brittle BMGs [15–18]. Therefore, despite their advantages, these amorphous alloys were unattractive for commercial applications due to lack of their ductility [19–23]. To improve ductility, two solutions have been

proposed: (a) the addition of alloy elements and (b) partial crystallization leading to the formation of amorphous matrix–nanocrystalline composite. Hence, in the last decade, numerous researchers tried to enhance the mechanical properties of Fe-based BMGs by the addition of alloy elements such as Cu [24], Ni [23], Zr [25], and Mo [26] or by the formation of nanocrystalline phases/precipitates in amorphous matrix [27–29]. In the case of partial annealing, it has been accepted that volume fraction, morphology, and type of crystalline precipitates have a strong effect on mechanical properties [30, 31]. Activation energy (E), the pre-exponential factor (A), and kinetic model ($g(\alpha)$) as the triple kinetic parameters are known as the essential information to control a reaction (such as crystallization); without knowing the kinetic parameters of this process, products of reactions can be uncontrollable. Therefore, kinetic analysis of partial annealing in BMGs (especially

✉ S. Hasani
hasani@yazd.ac.ir

¹ Department of Mining and Metallurgical Engineering, Yazd University, Yazd 89195-741, Iran

Fe-based BMGs) has attracted the attention of many researchers [32–37].

In recent years, $(\text{Fe}_{0.9}\text{Ni}_{0.1})_{77}\text{Mo}_5\text{P}_9\text{C}_{7.5}\text{B}_{1.5}$ BMG has been introduced as a Fe-based amorphous alloy with high ductility; furthermore, the effect of annealing treatment on the mechanical properties of this BMG was investigated [38, 39]. Nevertheless, despite the previous researches, no comprehensive investigation has been done into the kinetic analysis of crystallization process of this BMG and, therefore, there exists a knowledge gap. Therefore, non-isothermal kinetic analysis of crystallization process was investigated in $(\text{Fe}_{0.9}\text{Ni}_{0.1})_{77}\text{Mo}_5\text{P}_9\text{C}_{7.5}\text{B}_{1.5}]_{100-x}\text{Cu}_x$ ($x = 0.1$ at.%) BMG as a newer generation of Fe-based BMG in the present study. For this purpose, despite thermal, phase analysis, and microstructural observations, kinetic parameters of crystallization process in this BMG were calculated by different kinetic methods including the isoconversional Starink [40, 41] and Friedman (FR) [42] methods in combination with the invariant kinetic parameters (IKP) [43] and fitting methods [44].

Materials and methods

Materials and experimental procedure

The ingots of master alloy with the chemical compositions of $(\text{Fe}_{0.9}\text{Ni}_{0.1})_{77}\text{Mo}_5\text{P}_9\text{C}_{7.5}\text{B}_{1.5}]_{100-x}\text{Cu}_x$ ($x = 0.1$ at.%) were prepared in a vacuum arc furnace by melting the mixture of high purity (99.99 mass%) elements under a Ti gettered and argon atmosphere. To guarantee the homogeneity of the as-cast samples, all ingots were remelted for at least four times. Then, the initial metallic glassy alloys were prepared as rods with a diameter of 2 mm and a length of 100 mm by suction casting in a water-cooled Cu mold under high purity argon atmosphere. The chemical composition of the as-cast alloy was checked by inductively coupled plasma optical spectroscopy (ICP-OS) (presented in Table 1). As seen, the chemical composition of the BMG is in good agreement with the nominal composition.

The thermal behavior of BMG during crystallization processes was determined by a DTA (BAHR-STA 504) at an ambient temperature up to 1473 K, using various heating rates of 10, 20, and 40 K min^{-1} under high purity argon flow

Table 1 Chemical composition of the studied BMG (measured by ICP-OS)

Elements	Fe	Ni	Mo	P	C	B	Cu
Composition/at.%	68.5	7.4	4.7	9.3	8.8	1.2	0.1

supplied at a rate of 30 mL min^{-1} . According to DTA curves, the various stages of crystallization process in the BMG under non-isothermal condition were determined. Then, the samples of $(\text{Fe}_{0.9}\text{Ni}_{0.1})_{77}\text{Mo}_5\text{P}_9\text{C}_{7.5}\text{B}_{1.5}]_{100-x}\text{Cu}_x$ ($x = 0.1$ at.%) BMGs were annealed in non-isothermal condition by DTA at a heating rate of 20 K min^{-1} up to the temperature of each peak under argon flow. Phase analysis of the as-cast and annealed specimens was done by XRD (X'Pert MPD Philips Diffractometer) to determine the amorphous or crystalline phases. These results were recorded on an X'Pert MPD Philips diffractometer fitted with diffracted-beam monochromator set for Cu $k\alpha$ radiation ($\lambda = 0.1540$ nm) by “Brag Brentano” geometry. The operation voltage, current, scan speed, and step size were 45 kV, 40 mA, 1 s, and 0.05°, respectively. Furthermore, microstructural observations of the annealed samples were investigated by an FESEM (MIRA3 TESCAN). For this purpose, the surface of all the annealed specimens was polished by silicon carbide papers (up to 3000#) and then electrochemically etched by a 1 mol L^{-1} HCl and 0.5 mol L^{-1} H_2SO_4 solution operated at a potential of 3 V.

Kinetic analysis

To determine the kinetic parameters, isoconversional methods are usually used in association with IKP and Fitting [43] methods. Therefore, a significant number of researches [36, 44–46] investigated the kinetics analysis of solid-state reactions by the model-free (isoconversional) as well as model-fitting whose basis is discussed in the following.

Isoconversional methods

Isoconversional methods are used to determine E and its dependence on α [47–49]. The basis of these methods has been discussed in our previous articles [36, 45, 46]. Among these methods, Starink [41] and FR [42] methods are known as more accurate integral and differential isoconversional methods, respectively [50]. Hence, these two methods are discussed below.

1. The integral isoconversional Starink method [41] is a new method for the derivation of E_{α} , as follows:

$$\ln \frac{\beta}{T^{1.92}} = \text{const.} - 1.0008 \frac{E}{RT} \quad (1)$$

where α is the degree of conversion, β is the linear heating rate (K min^{-1}), T_{is} is the absolute temperature (K), R is the general gas constant ($\text{J mol}^{-1} \text{K}^{-1}$), and E is the activation energy (kJ mol^{-1}).

2. The differential isoconversional FR method [42] is a linear differential isoconversional method which is directly based on Eq. (2):

$$\ln \left[\beta \left(\frac{d\alpha}{dT} \right) \right] = \ln [A f(\alpha)] - \frac{E}{RT} \quad (2)$$

For a constant α , the plots $\ln(\beta/T^{1.92})$ versus $1/T$; and $\ln[\beta (d\alpha/dT)]$ versus $1/T$ recorded at several heating rates (at least for three heating rates) should be straight lines and the slope of each plot lets us calculate the E parameter by Starink and FR methods, sequentially.

IKP method

IKP method needs various α - T curves recorded at different heating rates. In this method, the invariant kinetic parameters including E_{inv} and A_{inv} values are achieved through the intersections of the curves of $\ln A$ versus E ; this intersection is observed for the correct kinetic models. Therefore, this method is based on the existence of a linear correlation between E and $\ln A$ [Eq. (3)] achieved by theoretical kinetic models.

$$\ln A_i = a + bE_i \quad (3)$$

In Eq. (3), subscript “ i ” indicates a value of heating rate and, a and b are the compensation effect parameters.

According to Eq. (4), for each theoretical kinetic model, the values of E and $\ln A$ are obtained from the slope and interruption of $\ln [g(\alpha)/T^2]$ versus $1/T$ plots, respectively. These algebraic expressions for the most frequently mechanisms have been presented in previous publications [51, 52].

$$\ln \frac{g(\alpha)}{T^2} \cong \ln \frac{AR}{\beta E} - \frac{E}{RT} \quad (4)$$

Fitting models

To validate the results obtained by isoconversional and IKP methods, fitting models are usually used [36, 44, 53]. In one of these methods, the reaction model can be established by plotting the numerical $g(a)$ based on theoretical and experimental data and finding the best matching between them. Therefore, the results obtained by this method can determine how and when the reaction mechanism changes during the course of transformation. The theoretical curves of $g(a)$ versus a are plotted according to the algebraic expressions for $g(a)$ used to describe the solid-state reactions (which have been presented elsewhere [44, 54]). While the experimental curve of $g(a)$ versus a is plotted by Eq. (5).

$$g(\alpha) = \frac{A}{\beta} \int_0^T \exp\left(-\frac{E}{RT}\right) dT \quad (5)$$

The temperature integral in Eq (5) ($\int_0^T \exp(-\frac{E}{RT}) dT$) is determined by Eq. (6) obtained by the Gorbachev approximation [55].

$$\int_0^T \exp\left(-\frac{E}{RT}\right) dT = \frac{RT^2}{E + 2RT} \exp\left(-\frac{E}{RT}\right) \quad (6)$$

Results and discussion

Experimental observations

Thermal analysis techniques including DTA, thermogravimetry (TG), differential scanning calorimetry (DSC), dilatometry (DIL), etc. are powerful and convenient methods to study the reactions at different heating rates [56–59]. Figure 1a shows the DTA curves of

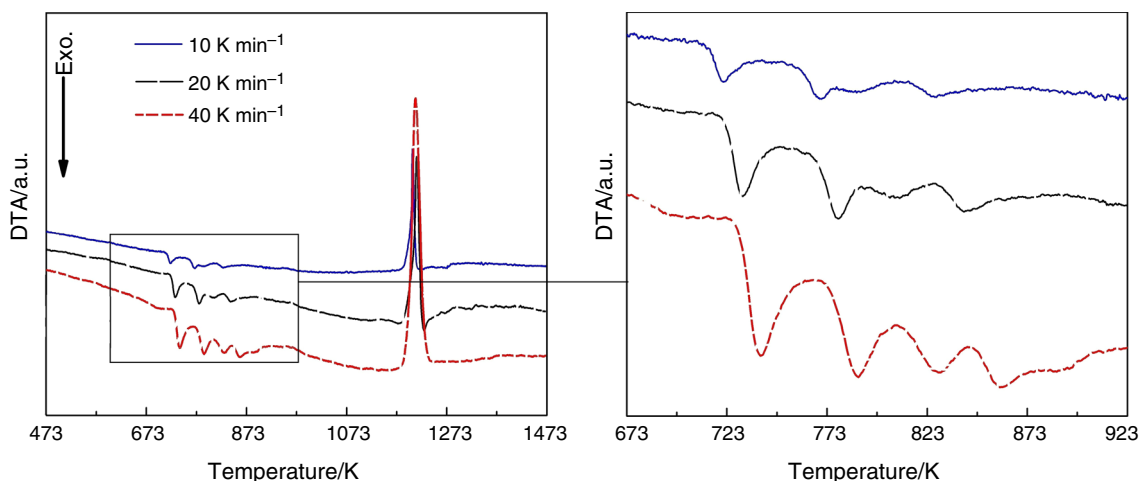


Fig. 1 DTA curves for the investigated BMG at different heating rates

[(Fe_{0.9}Ni_{0.1})₇₇Mo₅P₉C_{7.5}B_{1.5}]_{100-x}Cu_x (x = 0.1 at.%) BMG in four crystallization steps at various heating rates of 10, 20, and 40 K min⁻¹. As shown, with an increase in the heating rate, critical temperatures such as peak temperature (T_p), glass transition temperature (T_g), and one-set crystallization temperature (T_x) shift to higher temperature ranges which are in good agreement with the results obtained by other researcher [49, 50]. According to temperature ranges extracted from DTA curve at a heating rate of 20 K min⁻¹, related to the crystallization peaks, the as-cast specimens were annealed from ambient temperature up to 731, 778, 809, and 841 K at a heating rate of 20 K min⁻¹. Figure 2 depicts the X-ray diffraction patterns of the as-cast and annealed samples. As seen, in both the as-cast and the sample annealed at 731 K, just a broad single peak (in a range of $2\theta = 40\text{--}60$) is observed, indicating the amorphous nature and absence of crystalline phases in these samples. While, with an increase in the crystallization temperature to 841 K, some crystalline phases such as α -Fe, γ -Fe, FeNi₂P, and Fe₃C are formed, so that by annealing at a higher temperature, only the intensity of these crystalline phases is increased. Furthermore, the

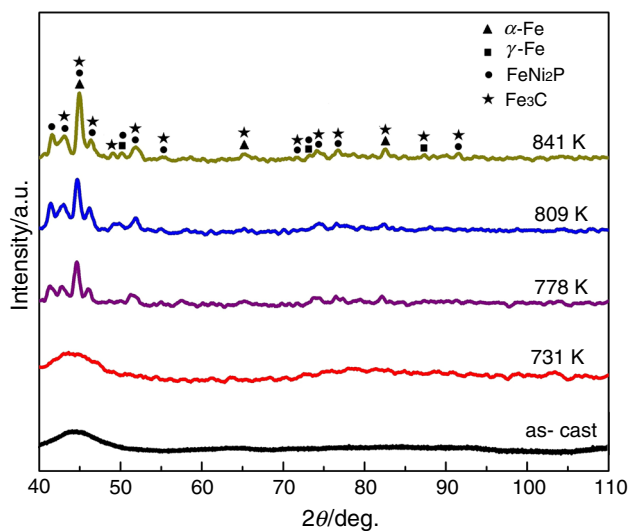


Fig. 2 XRD patterns of the as-cast and annealed specimens from ambient temperature up to various temperatures at a heating rate of 20 K min⁻¹

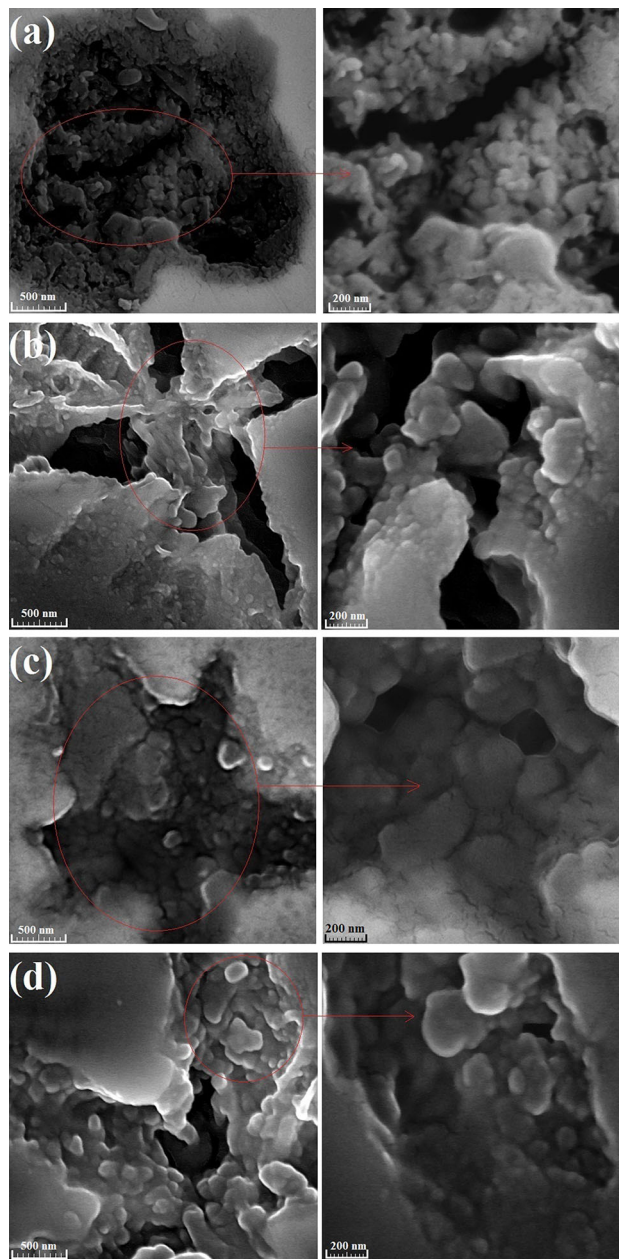


Fig. 3 FE-SEM micrographs of specimens annealed from ambient temperature up to **a** 731, **b** 778, **c** 809, and **d** 841 K at a heating rate of 20 K min⁻¹

Table 2 Volume fraction and average size of crystalline phases formed during annealing process at various temperatures

Annealing temperature/ K	Crystalline phase/ %	Average grain size calculated by Debye–Scherer method/nm	Average grain size obtained by MIP/ nm
731	–	42 ± 5	38 ± 3
778	9.2	59 ± 5	57 ± 5
809	15.4	67 ± 5	64 ± 6
841	20.2	84 ± 5	81 ± 6

volume fraction of crystalline phases was calculated by the rate of the peak's areas to the total area of the XRD pattern [51] as presented in Table 2. As shown, Table 2 clearly demonstrates that with an increase in the crystallization temperature from 778 to 841 K, the volume fraction of the crystalline phases increases from 9.2 to 20.2%. Furthermore, the average sizes of crystallites related to the samples annealed at various temperatures were calculated by the Debye–Scherer method [52] as shown in Eq. (7):

$$D = \frac{K\lambda}{\beta \cos \theta} \quad (7)$$

where for a constant K ($= 0.89$), D is the average grain size, λ is the X-ray wavelength ($\lambda \approx 1.5456 \text{ \AA}$), θ is the diffraction angle of the peak, and β is the full width at the half maximum of the peaks. The average of crystallite sizes of the annealed samples is presented in Table 2.

Also, Fig. 3a–c presents the micrographs of nano-crystalline phases related to the specimens annealed at various temperatures. To validate the Debye–Scherer results, the average size of crystalline phases was measured using the microstructural image processor (MIP) commercial software (presented in Table 2). As seen, with an increase in the crystallization temperature, the average grain size of crystalline phases is increased which is in good agreement with the Debye–Scherer results.

Kinetic calculations

Figure 4 shows the plots of α versus T at various heating rates (10, 20, and 40 K min^{-1}) for the four steps of crystallization process. To calculate local E , Starink and FR

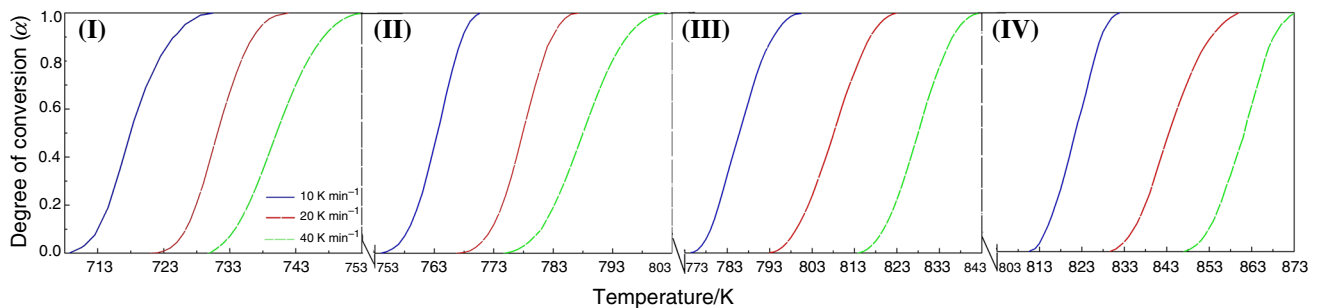


Fig. 4 Plots of α versus T at different heating rates for four crystallization stages

Table 3 Values of kinetic parameters obtained by isoconversional, IKP, and fitting methods

Peak no.	Isoconversional method $E/\text{kJ mol}^{-1}$		IKP method			Fitting method	
	Starink	Friedman	$E/\text{kJ mol}^{-1}$	$\ln A/\text{min}^{-1}$	r^2	$\ln A/\text{min}^{-1}$	Model
I	264 ± 8	257 ± 9	250 ± 13	41 ± 3	0.9999	44 ± 2	A_4
II	265 ± 11	263 ± 3	281 ± 11	46 ± 3	0.9998	40 ± 2	A_4
III	166 ± 1	171 ± 10	192 ± 6	28 ± 2	0.9989	25 ± 3	A_4
IV	190 ± 4	185 ± 1	201 ± 14	28 ± 3	0.9999	28 ± 2	P_4

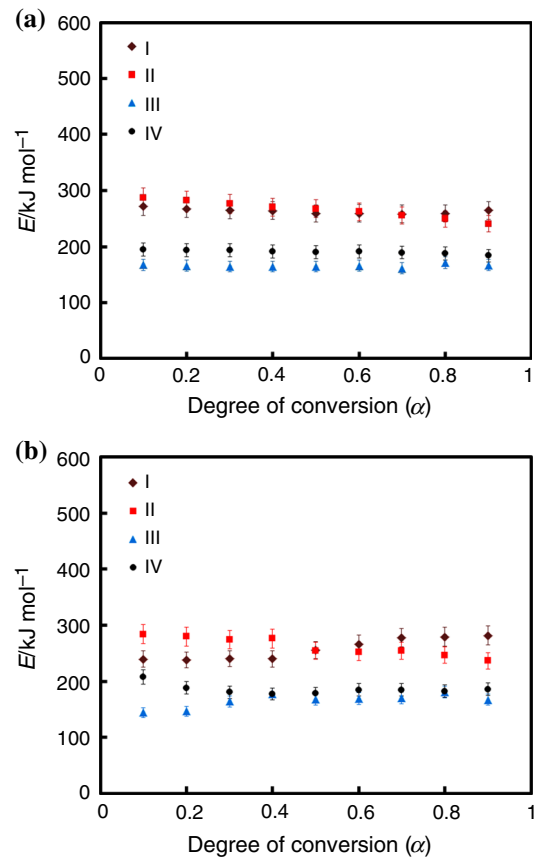


Fig. 5 The dependence of E on α evaluated for the non-isothermal crystallization process calculated by **a** Starink, and **b** FR methods

isoconversional kinetic methods were used; the plots of E versus α for all the four crystallization steps are shown in Fig. 5. As seen, within a wide range of α ($0.1 < \alpha < 0.9$),

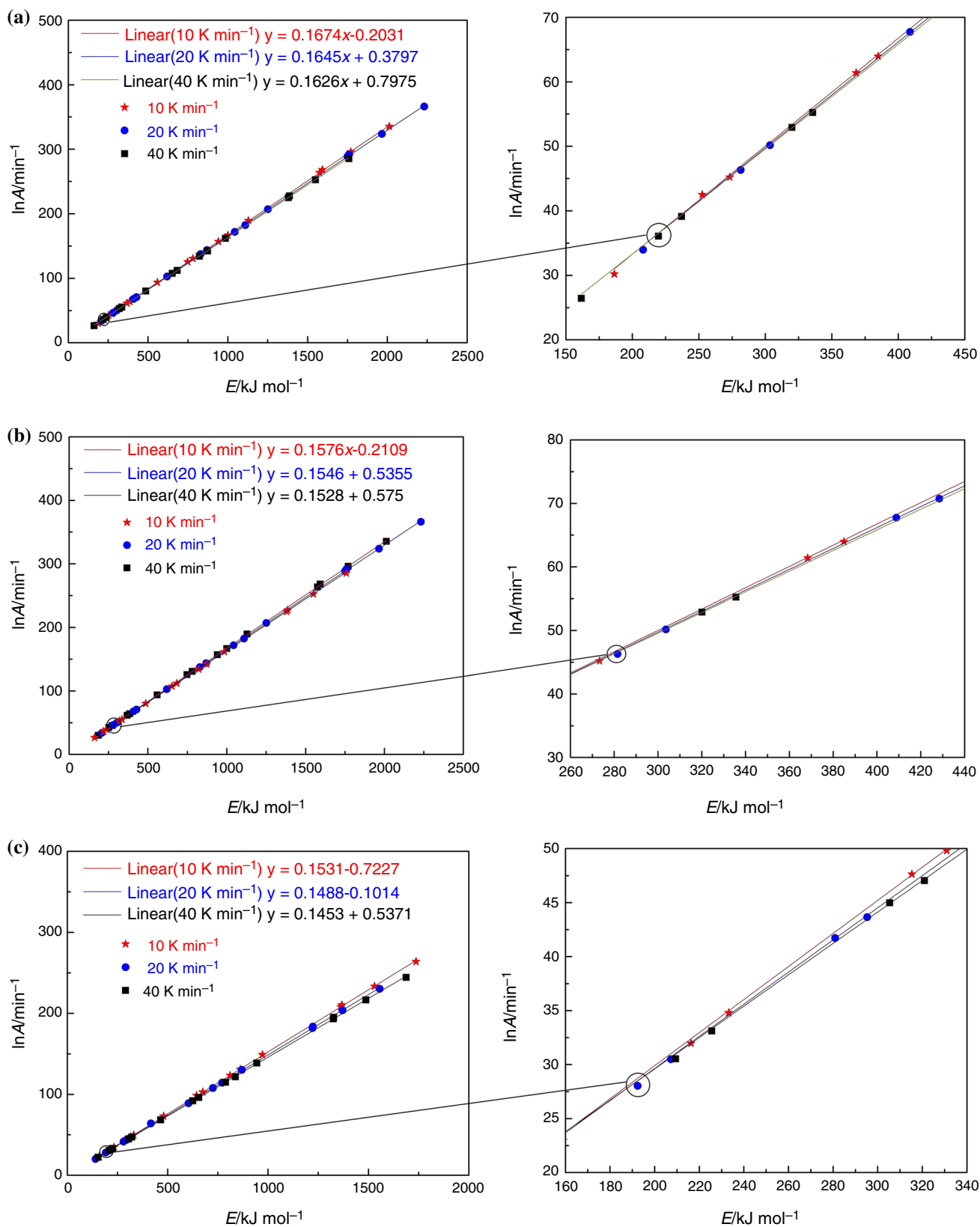


Fig. 6 The compensation relationship and enlarged region of interception for **a** I, **b** II, **c** III, and **d** IV crystallization peaks through IKP method

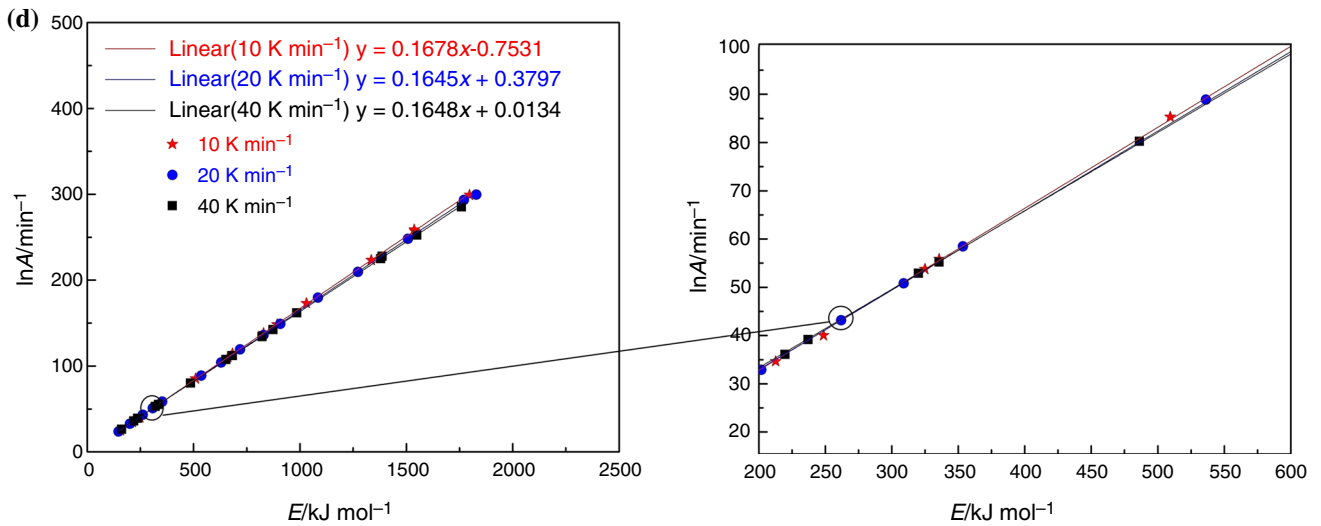


Fig. 6 continued

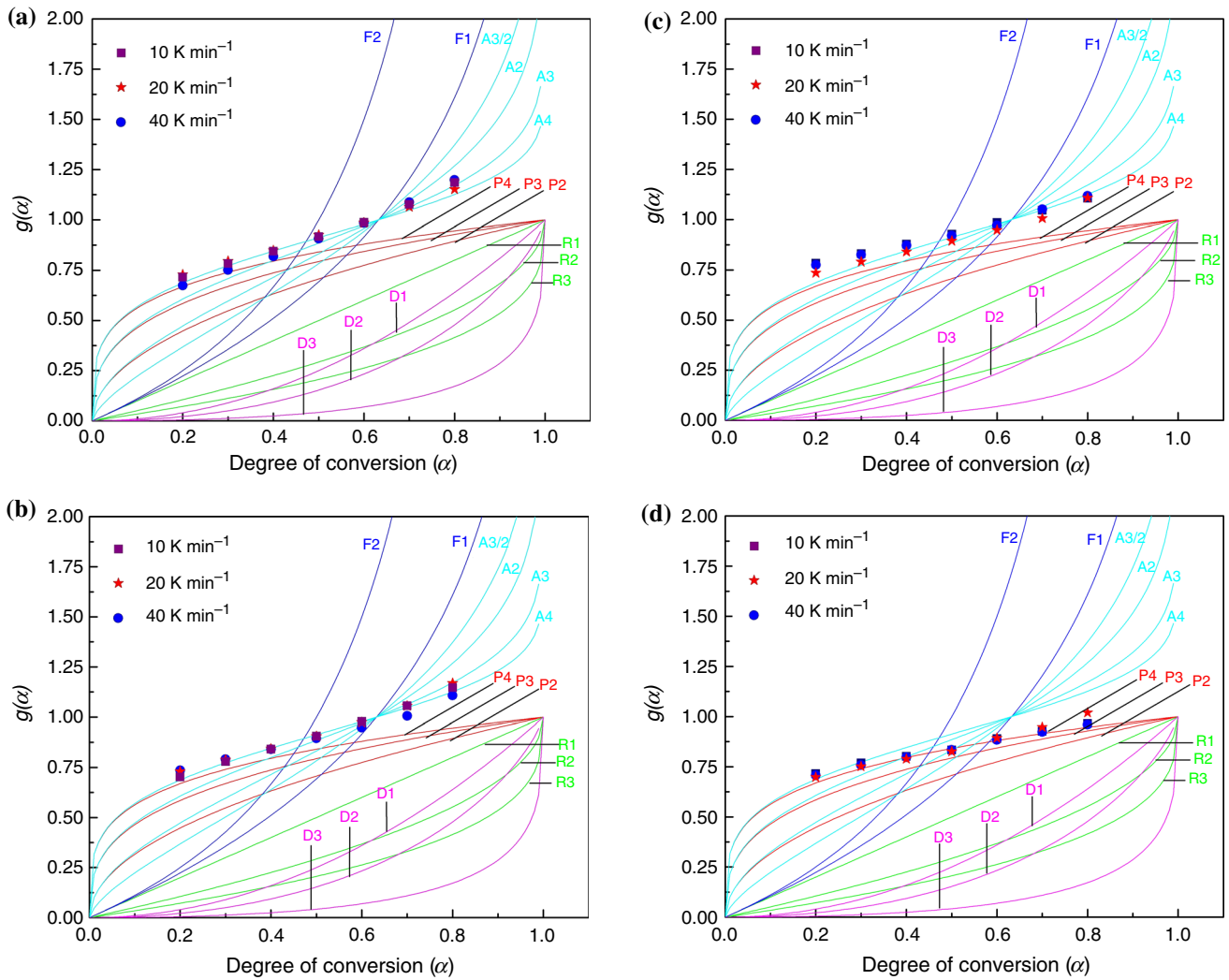


Fig. 7 The experimental and theoretical $g(\alpha)$ versus α plots for a I, b II, c III, and d IV crystallization peaks

the local activation energy related to each crystallization peak is practically independent on α . It means that all crystallization steps are one-step and controlled by a unique kinetic mechanism. The average of activation energies calculated by these isoconversional methods is presented in Table 3. As shown, the activation energies calculated by both Starink and FR methods are in good agreement with each other. Furthermore, it is found that the activation energies decrease with an increase in annealing temperature. Therefore, the formation of crystalline phases in the first and second crystallization stages faces higher energy barriers compared with the crystallites formed in the third and fourth stages.

The activation energies and the pre-exponential factors obtained by Coats–Redfern (CR) equation [60] were used for each crystallization stage and at each heating rate to determine other two kinetic parameters and to plot the linear relationship between $\ln A$ and E . For each stage, the linear relationship between $\ln A$ and E is shown in Fig. 6. As seen, the intersections of $\ln A$ versus E curves determine the correct activation energy, pre-exponential factor, and kinetic model. The results are presented in Table 3. These results confirm what has been achieved by isoconversional methods. In addition, it is revealed that the first, second, third, and fourth crystallization stages are controlled by A_4 , A_4 , A_4 , and P_4 models.

Furthermore, a popular fitting method was used to ensure the results obtained using the isoconversional and IKP methods. Figure 7 shows the theoretical and experimental $g(\alpha)$ versus α curves for each crystallization stage and heating rate. Also, the results extracted from these curves are presented in Table 3 which confirm the results obtained by other kinetic methods. According to kinetic models obtained, it is clear that nucleation and growth of nanocrystals control the crystallization process in Fe–Ni-based BMG.

Conclusions

In the present study, non-isothermal kinetic analysis of the crystallization process in the $[(\text{Fe}_{0.9}\text{Ni}_{0.1})_{77}\text{Mo}_5\text{P}_9\text{C}_{7.5}\text{B}_{1.5}]_{100-x}\text{Cu}_x$ ($x = 0.1$ at.%) BMG was investigated at different heating rates up to 1473 K. The research findings revealed that:

- DTA results showed that crystallization and melting processes took place in four exothermic peaks and one endothermic peak, respectively. The critical temperatures such as T_p , T_g , and T_x increased with an increase in the heating rate.
- The XRD results confirmed the occurrence of crystallization. These patterns illustrated that the crystalline

phases including α -Fe, γ -Fe, FeNi_2P , and Fe_3C were formed up to ~ 841 K. The average sizes of crystallites formed during the crystallization process at various temperatures (calculated by the Debye–Scherer method) were in the range of 40–80 nm.

- The average size of the nanocrystalline phases increased from 38 to 81 nm by increasing the crystallization temperature from 731 to 841 K. In addition, by increasing the crystallization temperature, the volume fraction of crystallized phases increased from 9.2 to 20.2%.
- Investigation of E diagram versus α for the crystalline phases in four crystallization steps indicated that E was approximately independent of α , within the conversion range of $0.10 \leq \alpha \leq 0.90$.
- Activation energy was calculated for every stage of crystallization by isoconversional Starink and Friedman methods. For instance, the activation energies calculated by Starink method were equal to 264, 265, 166, and 190 kJ mol^{-1} for the first, second, third and fourth crystallization stages, respectively.
- The results obtained by isoconversional methods were checked by IKP and fitting methods. The pre-exponential factors (A) calculated by IKP and Fitting methods were in a perfect agreement with each other.
- Kinetic models obtained from the two methods (IKP and Fitting) in different crystallization stages indicated that the four crystallization steps were controlled by the mechanisms of A_4 , A_4 , A_4 , and P_4 , respectively.

References

1. Inoue A, Wang X. Bulk amorphous FC20 (Fe–C–Si) alloys with small amounts of B and their crystallized structure and mechanical properties. *Acta Mater.* 2000;48:1383–95.
2. Long ZL, Shao Y, Deng XH, Zhang ZC, Jiang Y, Zhang P, et al. Cr effects on magnetic and corrosion properties of Fe–Co–Si–B–Nb–Cr bulk glassy alloys with high glass-forming ability. *Intermetallics.* 2007;15:1453–8.
3. Guo SF, Chan KC, Xie SH, Yu P, Huang YJ, Zhang HJ. Novel centimeter-sized Fe-based bulk metallic glass with high corrosion resistance in simulated acid rain and seawater. *J Non Cryst Solids.* 2013;369:29–33.
4. Pang SJ, Zhang T, Asami K, Inoue A. Synthesis of Fe–Cr–Mo–C–B–P bulk metallic glasses with high corrosion resistance. *Acta Mater.* 2002;50:489–97.
5. Dan Z, Makino A, Hara N. Effects of P addition on corrosion properties of soft magnetic FeSiB alloys. *Mater Trans.* 2013;54:1691–6.
6. Han Y, Kong FL, Han FF, Inoue A, Zhu SL, Shalaan E, et al. New Fe-based soft magnetic amorphous alloys with high saturation magnetization and good corrosion resistance for dust core application. *Intermetallics.* 2016;76:18–25.

7. Jung HY, Stoica M, Yi S, Kim DH, Eckert J. Electrical and magnetic properties of Fe-based bulk metallic glass with minor Co and Ni addition. *J Magn Magn Mater*. 2014;364:80–4.
8. Shen BL, Inoue A. Soft magnetic properties of bulk nanocrystalline Fe–Co–B–Si–Nb–Cu alloy with high saturated magnetization of 1.35 T. *J Mater Res*. 2004;19:2549–52.
9. Qi T, Li Y, Takeuchi A, Xie G, Miao H, Zhang W. Soft magnetic $\text{Fe}_{25}\text{Co}_{25}\text{Ni}_{25}(\text{B}, \text{Si})_{25}$ high entropy bulk metallic glasses. *Intermetallics*. 2015;66:8–12.
10. Lesz S, Kwapuliński P, Nabiałek M, Zackiewicz P, Hawelek L. Thermal stability, crystallization and magnetic properties of Fe–Co-based metallic glasses. *J Therm Anal Calorim*. 2016;125:1143–9.
11. Ferenc J, Kowalczyk M, Cie G. Magnetostrictive iron-based bulk metallic glasses for force sensors. *IEEE Trans Magn*. 2014;50:4–7.
12. Ramanan VRV. Metallic glasses in distribution transformer applications: an update. *J Mater Eng*. 1991;13:119–27.
13. Kim SW, Namkung J, Kwon O. Manufacture and industrial application of Fe-based metallic glasses. *Mater Sci Forum*. 2012;709:1324–30.
14. Makino A, Kubota T, Makabe M, Chang C, Inoue A. Fe-metalloid metallic glasses with high magnetic flux density and high glass-forming ability. *Mater Sci Forum*. 2007;565:1361–6.
15. Wang G, Zhao DQ, Bai HY, Pan MX, Xia AL, Han BS, et al. Nanoscale periodic morphologies on the fracture surface of brittle metallic glasses. *Phys Rev Lett*. 2007;98:235501.
16. Wu Y, Li HX, Jiao ZB, Gao JE, Lu ZP. Size effects on the compressive deformation behaviour of a brittle Fe-based bulk metallic glass. *Philos Mag Lett*. 2010;90:403–12.
17. Lewandowski JJ, Wang WH, Greer AL. Intrinsic plasticity or brittleness of metallic glasses. *Philos Mag Lett*. 2005;85:77–87.
18. Rezaei-Shahreza P, Seifoddini A, Hasani S. Microstructural and phase evolutions: their dependent mechanical and magnetic properties in a Fe-based amorphous alloy during annealing process. *J Alloys Compd*. 2017;738:197–205.
19. Hofmann DC. Bulk metallic glasses and their composites: a brief history of diverging fields. *J Mater*. 2013;2013:1–8.
20. Zhang T, Liu F, Pang S, Li R. Ductile Fe-based bulk metallic glass with good soft-magnetic properties. *Mater Trans*. 2007;48:1157–60.
21. Guo SF, Qiu JL, Yu P, Xie SH, Chen W. Fe-based bulk metallic glasses: brittle or ductile? *Appl Phys Lett*. 2014;105:161901.
22. Gu XJ, Poon SJ, Shiflet GJ. Mechanical properties of iron-based bulk metallic glasses. *J Mater Res*. 2007;22:344–51.
23. Yang W, Liu H, Zhao Y, Inoue A, Jiang K, Huo J, et al. Mechanical properties and structural features of novel Fe-based bulk metallic glasses with unprecedented plasticity. *Sci Rep*. 2014;4:6233.
24. Li X, Kato H, Yubuta K, Makino A, Inoue A. Effect of Cu on nanocrystallization and plastic properties of FeSiBPCu bulk metallic glasses. *Mater Sci Eng A*. 2010;527:2598–602.
25. Naitoh Y, Bitoh T, Hatanai T, Makino A, Inoue A. Application of nanocrystalline soft magnetic Fe–M–B (M = Zr, Nb) alloys to choke coils. *J Appl Phys*. 1998;83:6332–4.
26. Yang X, Ma X, Li Q, Guo S. The effect of Mo on the glass forming ability, mechanical and magnetic properties of FePC ternary bulk metallic glasses. *J Alloys Compd*. 2013;554:446–9.
27. Dou L, Liu H, Hou L, Xue L, Yang W, Zhao Y, et al. Effects of Cu substitution for Fe on the glass-forming ability and soft magnetic properties for Fe-based bulk metallic glasses. *J Magn Magn Mater*. 2014;358–359:23–6.
28. Bitoh T, Shibata D. Improvement of soft magnetic properties of $[(\text{Fe}_{0.5}\text{Co}_{0.5})_{0.75}\text{B}_{0.20}\text{Si}_{0.05}]_{96}\text{Nb}_4$ bulk metallic glass by B_2O_3 flux melting. *J Appl Phys*. 2008;103:07E702.
29. Stoica M, Roth S, Eckert J, Schultz L, Baró MD. Bulk amorphous FeCrMoGaPCB: preparation and magnetic properties. *J Magn Magn Mater*. 2005;290–291:1480–2.
30. Wang J, Li R, Hua N, Huang L, Zhang T. Ternary Fe–P–C bulk metallic glass with good soft-magnetic and mechanical properties. *Scr Mater*. 2011;65:536–9.
31. Zhang S, Sun D, Fu Y, Du H. Recent advances of superhard nanocomposite coatings: a review. *Surf Coat Technol*. 2003;167:113–9.
32. Joraid AA, El-oyoun MA, Alamri SN. Nonisothermal crystallization kinetics of amorphous $\text{Te}_{51.3}\text{As}_{45.7}\text{Cu}_3$. *Thermochim Acta*. 2008;470:98–104.
33. Liavitskaya T, Vyazovkin S. Kinetics of thermal polymerization can be studied during continuous cooling. *Macromol Rapid Commun*. 2017;39:1700624.
34. Ke HB, Xu HY, Huang HG, Liu TW, Zhang P, Wu M, et al. Non-isothermal crystallization behavior of U-based amorphous alloy. *J Alloys Compd*. 2017;691:436–41.
35. Stanford VL, Vyazovkin S. Thermal decomposition kinetics of malonic acid in the condensed phase. *Ind Eng Chem Res*. 2017;56:7964–70.
36. Rezaei-Shahreza P, Seifoddini A, Hasani S. Non-isothermal kinetic analysis of nano-crystallization process in $(\text{Fe}_{41}\text{Co}_7\text{Cr}_{15}\text{Mo}_{14}\text{Y}_2\text{C}_{15})_{94}\text{B}_6$ amorphous alloy. *Thermochim Acta*. 2017;652:119–25.
37. Wang X, Zeng M, Nollmann N, Wilde G, Wang J, Tang C. Thermal stability and non-isothermal crystallization kinetics of $\text{Pd}_{82}\text{Si}_{18}$ amorphous ribbon. *AIP Adv*. 2017;7:065206.
38. Seiffodini A, Zaremehrdardi S. Effects of heat treatment on crystallization behavior, microstructure and the resulting microhardness of a $(\text{Fe}_{0.9}\text{Ni}_{0.1})_{77}\text{Mo}_5\text{P}_9\text{C}_{7.5}\text{B}_{1.5}$ bulk metallic glass composite. *J Non Cryst Solids*. 2016;432:313–8.
39. Askari-paykani M, Ahmadabadi MN, Seiffodini A. The effect of liquid phase separation on the Vickers microindentation shear bands evolution in a Fe-based bulk metallic glass. *Mater Sci Eng A*. 2013;585:363–70.
40. Starink MJ. Activation energy determination for linear heating experiments: deviations due to neglecting the low temperature end of the temperature integral. *J Mater Sci*. 2006;42:483–9.
41. Starink M. The determination of activation energy from linear heating rate experiments: a comparison of the accuracy of iso-conversion methods. *Thermochim Acta*. 2003;404:163–76.
42. Friedman HL. Kinetics of thermal degradation of char-forming plastics from thermogravimetry. Application to a phenolic plastic. *J Polym Sci Part C Polym Symp*. 2007;6:183–95.
43. Lesnikovich AI, Levchik SV. A method of finding invariant values of kinetic parameters. *J Therm Anal*. 1983;27:89–93.
44. Hasani S, Shamanian M, Shafyei A, Behjati P, Szpunar JAA. Non-isothermal kinetic analysis on the phase transformations of Fe–Co–V alloy. *Thermochim Acta*. 2014;596:89–97.
45. Rezaei-Shahreza P, Seifoddini A, Hasani S. Thermal stability and crystallization process in a Fe-based bulk amorphous alloy: the kinetic analysis. *J Non Cryst Solids*. 2017;471:286–94.
46. Hasani S, Panjepour M, Shamanian M. Non-isothermal kinetic analysis of oxidation of pure aluminum powder particles. *Oxid Met*. 2013;81:299–313.
47. Ledeti A, Olariu T, Caunii A, Vlase G, Circioban D, Baul B, et al. Evaluation of thermal stability and kinetic of degradation for levodopa in non-isothermal conditions. *J Therm Anal Calorim*. 2018;131:1881–8.
48. Prajapati R, Kasyap S, Patel AT, Pratap A. Non-isothermal crystallization kinetics of $\text{Zr}_{52}\text{Cu}_{18}\text{Ni}_{14}\text{Al}_{10}\text{Ti}_6$ metallic glass. *J Therm Anal Calorim*. 2016;124:21–33.
49. Uzun N, Colak AT, Emen FM, Cilgi GK. The thermal and detailed kinetic analysis of dipicolinate complexes. *J Therm Anal Calorim*. 2016;124:1735–44.

50. Campostrini R, Mahmoud A, Leoni M, Scardi P. Activation energy in the thermal decomposition of MgH_2 powders by coupled TG-MS measurements. *J Therm Anal Calorim.* 2014;116:225–40.
51. Criado JM. The use of the IKP method for evaluating the kinetic parameters and the conversion function of the thermal dehydrochlorination of PVC from non-isothermal data. *Polym Degrad Stab.* 2004;84:311–20.
52. Singh A, Sharma TC, Kishore P. Thermal degradation kinetics and reaction models of 1,3,5-triamino-2,4,6-trinitrobenzene-based plastic-bonded explosives containing fluoropolymer matrices. *J Therm Anal Calorim.* 2017;129:1403–14.
53. Vyazovkin S, Burnham AK, Criado JM, Pérez-Maqueda LA, Popescu C, Sbirrazzuoli N. ICTAC kinetics committee recommendations for performing kinetic computations on thermal analysis data. *Thermochim Acta.* 2011;520:1–19.
54. Aghili S, Panjepour M, Meratian M. Kinetic analysis of formation of boron trioxide from thermal decomposition of boric acid under non-isothermal conditions. *J Therm Anal Calorim.* 2018;131:2443–55.
55. Gorbachev VM, Lad KN, Savalia RT, Pratap A, Dey GK, Banerjee S. A solution of the exponential integral in the non-isothermal kinetics for linear heating. *J Therm Anal.* 1975;8:349–50.
56. Hasani S, Panjepour M, Shamanian M. Effect of atmosphere and heating rate on mechanism of MoSi_2 formation during self-propagating high-temperature synthesis. *J Therm Anal Calorim.* 2012;107:1073–81.
57. Souri D, Shahmoradi Y. Calorimetric analysis of non-crystalline $\text{TeO}_2\text{-V}_2\text{O}_5\text{-Sb}_2\text{O}_3$. Determination of crystallization activation energy, Avrami index and stability parameter. *J Therm Anal Calorim.* 2017;129:601–7.
58. Hasani S, Panjepour M, Shamanian M. A study of the effect of aluminum on MoSi_2 formation by self-propagation high-temperature synthesis. *J Alloys Compd.* 2010;502:80–6.
59. Gong P, Yao K, Zhao S. Cu-alloying effect on crystallization kinetics of $\text{Ti}_{41}\text{Zr}_{25}\text{Be}_{28}\text{Fe}_6$ bulk metallic glass. *J Therm Anal Calorim.* 2015;121:697–704.
60. Coats AW, Redfern JP. Kinetic parameters from thermogravimetric data. *Nature.* 1964;201:68–9.